Article

Self-Compensated Driving Circuit for Reducing Drift and Hysteresis in Force Sensing Resistors

Leonel Paredes-Madrid [1],* [iD], Johanna Fonseca [1] [iD], Arnaldo Matute [1] [iD], Elkin I. Gutiérrez Velásquez [1] [iD] and Carlos A. Palacio [2] [iD]

1   Faculty of Mechanic, Electronic and Biomedical Engineering, Universidad Antonio Nariño, Carrera 7 N 21–84, Tunja, Boyacá 150001, Colombia; johafonseca@uan.edu.co (J.F.); arnaldo.matute@uan.edu.co (A.M.); elkin.gutierrez@uan.edu.co (E.I.G.V.)

2   Faculty of Sciences, Universidad Antonio Nariño, Carrera 7 N 21–84, Tunja, Boyacá 150001, Colombia; carlospalacio@uan.edu.co

*   Correspondence: paredes.leonel@uan.edu.co; Tel.: +57-8744-7564

check for
updates

Abstract: Force Sensing Resistors (FSRs) are manufactured from a blend of conductive nanoparticles dispersed in an insulating polymer matrix. FSRs exhibit large amounts of hysteresis and drift error, but currently, a great effort is placed on improving their performance through different techniques applied during sensor manufacturing. In this article, a novel technique for improving the performance of FSRs is presented; the method can be applied to already-manufactured sensors, which is a clear benefit of the proposed procedure. The method is based on driving the sensors with a modified-astable 555 oscillator, in which the oscillation frequency is set from the sensor's capacitance and resistance. Considering that the sensor's capacitance and resistance have opposite signs in the drift characteristic, the driving circuit provides self-compensated force measurements over extended periods of time. The feasibility of the driving circuit to reduce hysteresis and to avoid sensitivity degradation is also tested. In order to obtain representative results, the experimental measurements from this study were performed over eight FlexiForce A201-25 sensors.

Keywords: driving circuit; force sensor; pressure sensor; tactile sensor; FSR; piezoresistive sensor

1. Introduction

Force Sensing Resistors (FSRs) offer versatile and cost-effective force readings to applications with space and weight constraints. FSRs can be fashioned into multiple shapes and dimensions to fulfill the requirements of a given final application [1–3]; this can be done by simply cutting the nanocomposite film after the production process is done, followed by electrode positioning and wiring to assemble the final force sensor [4]. The nanocomposite film is obtained by randomly dispersing conductive particles in an insulating polymer matrix [5–7]. Finally, when the sensor is assembled, a time-multiplexed circuit is employed to read out the sensor's resistance and provide a pressure profile map [4,8].

Nonetheless, FSRs have found limited acceptance in applications demanding accurate force readings due to the poor reproducibility of the piezoresistive behavior [9,10]. By taking a glance at the datasheets of commercial FSRs [11–13], they exhibit from ten to one hundred times more drift and hysteresis error than load cells. Fortunately, a great effort is currently placed on improving the performance of FSRs by investigating multiple trends such as the integration of carbon nanotubes in the polymer matrix [7,14], changing the electrode configuration of the assembled sensor [15,16], testing different types of polymers [17,18], and adding non-conductive nanoparticles to reinforce the polymer matrix with the aim of reducing creep [9].

On the other hand, previous authors' works have focused on a completely different approach to improve the accuracy of FSRs. The authors have developed a physical model for the quantum tunneling conduction of FSRs that comprises the series connection between multiple tunneling resistances (R^i_{bulk}) and contact resistances (R^i_c) [19]; this is depicted in the sketch of Figure 1a. The tunneling resistance takes place at the tunneling path of two particles separated by a potential barrier of width s and height V_a, where s is also known in the literature as the mean inter-particle separation. The polymer matrix acts as the insulating potential barrier in the nanocomposite; this is shown in Figure 1b.
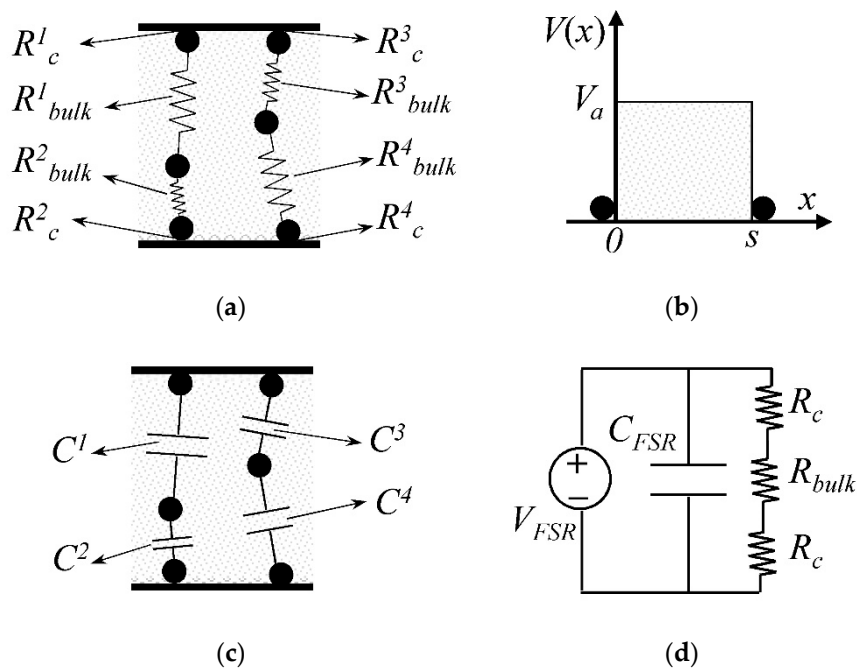

(a) (b) (c) (d)

Figure 1. The electric model of FSRs. (**a**) Sketch of the lumped resistances in an FSR representing the contact resistances (R^i_c) and the tunneling resistances (R^i_{bulk}); (**b**) representation of the tunneling resistance between two conductive particles separated by a potential barrier of height V_a and width s; (**c**) Sketch of the lumped capacitances (C^i) in an FSR; (**d**) Macroscopic model of an FSR connected to an external driving voltage (V_{FSR}), where R_c and R_{bulk} represent the net contact and tunneling resistances, respectively. The symbol C_{FSR} matches for the net capacitance of the FSR.

The contact resistance takes place between the sensor electrodes and the conductive particles, and between neighboring particles, but for simplicity, the sketch from Figure 1a only shows the former scenario. The particles shown in Figure 1a may be formed by nanoparticle agglomerates that behave as greater-microscopic-particles. These neighboring nanoparticles also exhibit contact resistance among them.

Both resistances, R^i_{bulk} and R^i_c, are stress-dependent but only R^i_{bulk} is modified by the driving voltage (V_{FSR}). A detailed discussion on the tunneling resistance, R^i_{bulk}, is later addressed in Section 2.1 Conversely, the contact resistance, R^i_c, only depends on the physical constriction occurring at the interface between two materials, and therefore, R^i_c is voltage-independent. Computer simulations and experimental results have demonstrated the validity of the authors' model in that it is able to predict a lower drift error for incremental values of V_{FSR} [20]. This implies that the drift error can be minimized by trimming V_{FSR} in the driving circuit. Note that this is opposed to what the manufacturers of FSRs have stated in their product datasheets [11–13], i.e., a constant drift error regardless of V_{FSR}.

Following the authors' model, the distributed capacitance can be found along the multiple tunneling paths of the nanocomposite; see Figure 1c. The total capacitance of an FSR can be computed from the multiple lumped capacitances (C^i) which are connected in series and in parallel. Similarly,

the total resistance of an FSR (R_{FSR}) can be computed from the series and parallel connections of $R^i{}_c$ and $R^i{}_{bulk}$, thus yielding R_c, and R_{bulk}; see Figure 1d. Previous authors' works have demonstrated that performing capacitance readings on FSRs yield a lower hysteresis error [21,22], this has been experimentally measured and also predicted by theoretical models which are later addressed in Section 2.3.

The development of a physical model for the current conduction of FSRs is of paramount importance for the definition of strategies that enhance the accuracy of such devices; this can be done in a two-folded strategy. From the standpoint of a nanocomposite designer, the physical model provides a full overview of the design parameters that impact the FSRs' performance the most. For instance, it may be interesting to simulate—prior to assembly—the influence of choosing carbon black or metallic particles as the nanocomposite filler. Multiple simulations can be performed with a wide range of design parameters, such as the mass ratio of nanoparticles to polymer, the type of polymer, the particles' dimensions and shape, etc. From the standpoint of a final user, the physical model aims to design the most appropriate driving circuit that maximizes the sensors' performance. Based on the latter statement, the target of this study is to design and test a driving circuit that minimizes—or even removes—most of the error sources of FSRs, where drift, hysteresis, and sensitivity degradation are the most important error sources.

The rest of this paper is organized as follows: Section 2 reviews the physical model, the error sources and the types of error in FSRs. A detailed design of the self-compensated driving circuit is presented in Section 3, followed by the experimental setup, results, and discussion in Section 4. Conclusions are stated in Section 5. With the aim of obtaining representative results, the experimental data from this study were collected from eight FlexiForce A201-25 sensors (Tekscan, Inc., Boston, MA, USA) manufactured from an elastomeric polymer, as the insulating phase, and carbon black nanoparticles as the conductive phase [23,24].

2. Review of the Underlying Physics and Important Definitions of FSRs

The authors' proposed model and experimental data from our previous works are presented here [19,20]. The authors' proposed model imposes a voltage-dependent behavior for the tunneling conduction of FSRs; this is radically different from well-known models in the literature [6,25,26]. The authors' proposed model has demonstrated its validity by predicting-up to some extent-the sensitivity degradation of Conductive Polymer Composites. Additionally, it predicts that the drift error is voltage-dependent, just as experimentally measured [19,20].

The main sensing mechanism of FSRs is the reduction of the mean inter-particle separation, s, when subjected to mechanical stress (σ), i.e., s is a stress-dependent function defined from

$$s = s_0(1 - \sigma/M), \tag{1}$$

where M is the compressive modulus of the nanocomposite and s_0 is the inter-particle separation when $\sigma = 0$. For incremental values of stress, s is proportionally reduced, but the tunneling resistance exhibits a dramatic decrement due to the non-linear behavior of quantum tunneling. The authors have demonstrated that additional factors have influence on the resistance changes; these are the contact resistance, R_c, and the effective area for tunneling conduction (A) [19]. They are briefly described ahead.

2.1. Physical Model for Quantum Tunneling Conduction of FSRs

From Figure 1d, the total resistance of an FSR can be computed from

$$R_{FSR} = R_{bulk} + 2R_c \tag{2}$$

If the FSR is sourced with a constant V_{FSR}, the voltage drop across the tunneling barrier (V_{bulk}) can be found from sensor current (I) and Equation (2) as

$$V_{bulk} = V_{FSR} - 2R_c I \tag{3}$$

In 1963, Simmons derived a set of piecewise equations for the quantum tunneling conduction through thin insulating films [27]. The piecewise intervals are defined as a function of V_{bulk}. The Simmons' equations can be arranged to estimate R_{bulk}. However, an analytic solution for R_{bulk} is only possible when $V_{bulk} \approx 0$. For larger values of V_{bulk}, only a numerical value can be found for R_{bulk}. The expressions relating V_{bulk} with I are presented next.

If $V_{bulk} \approx 0$

$$R_{bulk} = \frac{V_{bulk}}{I} = \frac{2s}{3A\sqrt{2mV_a}} \left(\frac{h}{e}\right)^2 \exp\left(\frac{4\pi}{h} s\sqrt{2mV_a}\right) \tag{4}$$

If $V_{bulk} < V_a/e$

$$I = \frac{Ae}{2\pi hs^2} \left\{ \left(V_a - \frac{eV_{bulk}}{2}\right) \exp\left[-\frac{4\pi}{h}s\sqrt{2m\left(V_a - \frac{eV_{bulk}}{2}\right)}\right] - \left(V_a + \frac{eV_{bulk}}{2}\right) \exp\left[-\frac{4\pi}{h}s\sqrt{2m\left(V_a + \frac{eV_{bulk}}{2}\right)}\right] \right\} \tag{5}$$

If $V_{bulk} > V_a/e$

$$I = \frac{2.2Ae^3 V_{bulk}^2}{8\pi h V_a s^2} \left\{ \exp\left[-\frac{8\pi s}{2.96heV_{bulk}}\sqrt{2mV_a^3}\right] - \left(1 + \frac{2eV_{bulk}}{V_a}\right)\exp\left[-\frac{8\pi s}{2.96heV_{bulk}}\sqrt{2mV_a^3\left(1 + \frac{2eV_{bulk}}{V_a}\right)}\right] \right\}, \tag{6}$$

where m and e are the electron mass and charge, respectively, and h is the Planck constant. The effective area for tunneling conduction, A, is a stress-dependent magnitude with experimentally-determined parameters A_0, A_1, and A_2 given by

$$A = A_0 + A_1 \sigma^{A_2} \tag{7}$$

In order to calculate R_{bulk} for Equations (5) and (6), it is necessary to replace Equation (3) and find a numerical solution. Then, the quotient $R_{bulk} = V_{bulk}/I$ can be computed. This procedure is not necessary for the interval of Equation (4). Note that Equations (5) and (6) impose a voltage-dependent behavior for the tunneling resistance, and consequently, the resulting errors, hysteresis, and creep, also depend on V_{FSR}; this is because the tunneling and the contact resistance have different dynamics as described next.

Mikrajuddin et al. [28] and Shi et al. [29] have found expressions for the constriction (contact) resistance that exists between electrodes of arbitrary sizes. In their work, the contact resistance follows power laws with fixed coefficients, but some modifications had to be introduced by the authors in order to account for the stress-dependent area of Equation (7). Finally, the contact resistance, R_c, can be found from

$$R_c = R_{par} + \frac{R_c^0}{\sigma^k}, \tag{8}$$

where R_{par} is the net resistance of the conductive particles dispersed in the insulating polymer matrix and R_c^0 and k are experimentally-measured parameters. The numerical value of the parameters R_c^0, k, A_0, A_1, and A_2 can be found in Reference [19] for the FlexiForce A201-1 (Tekscan, Inc., Boston, MA, USA) and the Interlink FSR 402 sensors (Interlink Electronics, Inc., Westlake Village, CA, USA) with nominal ranges of 4.5 N and 20 N, respectively. Figure 2 shows plots of R_{FSR}, R_{bulk}, and R_c as a function of V_{FSR} for two different mechanical loads. Note that R_{bulk} dominates for low V_{FSR}, whereas at large V_{FSR}, the contact resistance dominates; so if V_{FSR} is chosen accordingly, the dynamic behavior of R_{bulk} or R_c can be independently studied.
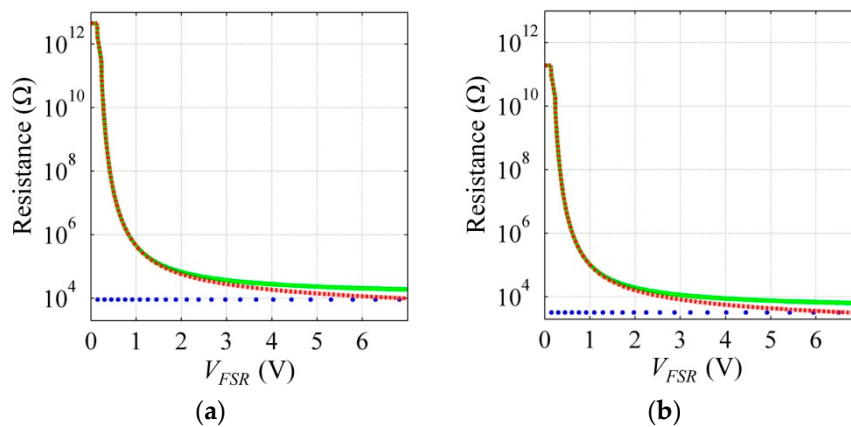
Figure 2. The simulation plot of R_{FSR} (solid green), R_{bulk} (dashed red), and R_c (blue points) as a function of V_{FSR} for two mechanical loads of (**a**) σ = 50 kPa and (**b**) σ = 500 kPa. The simulation is obtained for the FlexiForce A201-1 sensor from experimentally-measured parameters [19] and Equations (2)–(8).

It must be highlighted that the authors' model can be applied to any FSR operating on the basis of quantum tunneling; this is because Equations (2)–(8) are stated in terms of universal constants (m, h, e), and in terms of specific properties from the polymer and the conductive particles (V_a, M). The inter-particle separation is defined by the mass ratio between the conductive and insulating phases; this ratio is known in the literature as the filler volume fraction (ϕ) [6,25,26]. In general, the larger ϕ is, the more sensitive the sensor becomes, so the nominal range of an FSR can be trimmed by setting ϕ during manufacturing. The FlexiForce A201-25 sensor, with a nominal range of 110 N, has been assembled with a lower ϕ than the FlexiForce A201-1 which exhibits a nominal range of 4.5 N. Considering that both FlexiForce sensors are manufactured from the same materials, the overall shape of Figure 2 is held, with the only difference being that the FlexiForce A201-25 is less sensitive to applied stress due to the lower ϕ.

2.2. Physical Model for the Capacitance of FSRs.

The total capacitance of an FSR (C_{FSR}) can be computed from the series and parallel connections of the multiple lumped capacitances of Figure 1c. By definition, C_{FSR} can be calculated from

$$C_{FSR} = \varepsilon_r \varepsilon_0 A/s \tag{9}$$

where ε_0 and ε_r are the vacuum and relative permittivities, respectively. The parameters A and s have the same meaning from Section 2.1. The authors' previous work has demonstrated that C_{FSR} is voltage independent [30] as Equation (9) predicts.

2.3. Error Sources and Types of Error in FSRs

The main error source in FSRs is the viscoelastic response of the polymer matrix that causes hysteresis and creep in the inter-particle separation; this implies that s must be redefined from Equation (1) as a time (t) and stress-dependent function $s(\sigma,t)$. Several models are available in the literature for the viscoelasticity of polymers [31]. Some authors such as Zhang et al. [25] and Kalantari et al. [26] have combined the Kelvin–Voigt rheological model with Equation (4) obtaining overall good results. However, experimental observations from the authors have demonstrated that the creep phenomenon can be more accurately modeled if the whole set of Simmons' equations are combined with the Burgers model, i.e., by replacing $s(\sigma,t)$ in Equations (4)–(6). A detailed derivation of the authors' model for creep is available in Reference [20]. The model predicts a lower creep in sensor resistance, R_{FSR}, for incremental values of V_{FSR}. This can be understood from the fact that the

only source of creep is the inter-particle separation, so if V_{FSR} is large enough, the dominant role of R_c yields low creep because R_c does not depend on s, see Equation (8). Conversely, for low values of V_{FSR}, the tunneling resistance dominates, and therefore, a larger creep is predicted by the model because R_{bulk} does depend on s in an exponential fashion, see Equation (4).

When dealing with capacitance measurements over extended periods of time, polymer creep causes a reduction in the inter-particle separation that increases the sensor's capacitance; see Equation (9). This implies that capacitance drift is always positive and independent of V_{FSR}. In opposition, the creep in R_{FSR} is always negative, i.e., the sensor's resistance decreases over time. This is the key aspect for designing a self-compensated driving circuit.

It must be highlighted that lower drift is always measured in C_{FSR} than in R_{bulk} for a given specimen; this can be demonstrated by a comparison between Equation (9) and the expressions for R_{bulk}. For the sake of simplicity, only Equations (4) and (9) are compared here. Given a small reduction (ε) in the inter-particle separation due to polymer creep at time t_f, so that $s(\sigma, t_f) = s_i - \varepsilon$, where $s(\sigma, 0) = s_i$, readers can verify the validity of the following inequality:

$$\frac{1/(s_i) - 1/(s_i - \varepsilon)}{1/(s_i)} < \frac{s_i \exp(\gamma s_i) - (s_i - \varepsilon) \exp(\gamma(s_i - \varepsilon))}{s_i \exp(\gamma s_i)}, \tag{10}$$

where $\gamma = 4\pi(2mV_a)^{-1/2}/h$.

The inequality of Equation (10) can be understood as follows: due to the polymer creep, a small decrement in the inter-particle separation, ε, always produces a larger normalized variation in R_{bulk} than in C_{FSR} due to the exponential term of Equation (4). The same conclusion can be stated for the other voltage intervals of Equations (5) and (6). Concerning the hysteresis error, a similar demonstration to Equation (10) has been presented by the authors in Reference [22].

Besides creep and hysteresis, FSRs may exhibit sensitivity degradation when subjected to dynamic (cyclic) loading. Sensitivity degradation has been reported in multiple studies related to polymer nanocomposites. Some authors have reported it for custom-made stress [32,33] and strain sensors [34], thus indicating that sensitivity degradation is not exclusive of FlexiForce sensors [35,36], but rather, a phenomenon related with the polymer composite itself. The authors have experimentally demonstrated that sensitivity degradation is a voltage-related phenomenon that only occurs when the contact resistance is the main sensing mechanism of the FSR, i.e., when V_{FSR} is large enough [20]. Unfortunately, this explanation is not yet fully satisfactory because Equation (8) does not predict sensitivity degradation by itself. This implies that additional phenomena are occurring at a microscopic level that the authors' model does not account for. Up to now, the underlying basis of sensitivity degradation remains undisclosed and only hypotheses for this phenomenon have been provided. For instance, Canavesse et al. hypothesized that sensitivity degradation is caused by hysteresis [32]. A proven method to avoid sensitivity degradation is to set V_{FSR} as low as possible so that the main sensing mechanism of the FSRs is the variation of the inter-particle separation [20].

3. Design of a Self-Compensated Driving Circuit

When cyclic loading is applied to an FSR, sensitivity degradation and hysteresis are the main concerns, but when static loads are applied, drift is the main source of error. In order to design a self-compensated driving circuit, all these considerations must be taken into account.

The design methodology of this study gives the following importance order to the multiple types of error: first, sensitivity degradation, second, drift, and third, hysteresis.

With the aim of avoiding sensitivity degradation, V_{FSR} must be held as low as possible. The previous authors' work has demonstrated that sensitivity degradation may appear even at voltages of 3 V [20]. Unfortunately, there is not a universal threshold voltage for avoiding sensitivity degradation because conductive particles are randomly dispersed in the polymer matrix, and therefore, identical sensors do not exist. In order to minimize drift, the driving circuit must be designed so that capacitance creep is compensated by the resistance creep; this is not achievable in a straightforward manner as predicted

by the inequality of Equation (10), so an offset is required to compensate for the larger creep in sensor's resistance, R_{FSR}.

Based upon the previous statements, the driving circuit of Figure 3 is proposed with *Vcc* set to 2.5 V which is the lowest admissible supply voltage for the 555 device. In addition, the voltage across the FSR never goes beyond $2/3 \cdot Vcc$ due to the operation principle of the 555. Given the low *Vcc*, Shottky diodes should be used instead of regular diodes. The circuit output (D_o) is a square signal with frequency *f* that changes accordingly with the applied stress. Measuring and correlating *f* with the applied stress is the sensing mechanism of the circuit in Figure 3. A comparison between the classical version of the astable oscillator and the circuit of Figure 3 is addressed in Appendix A.
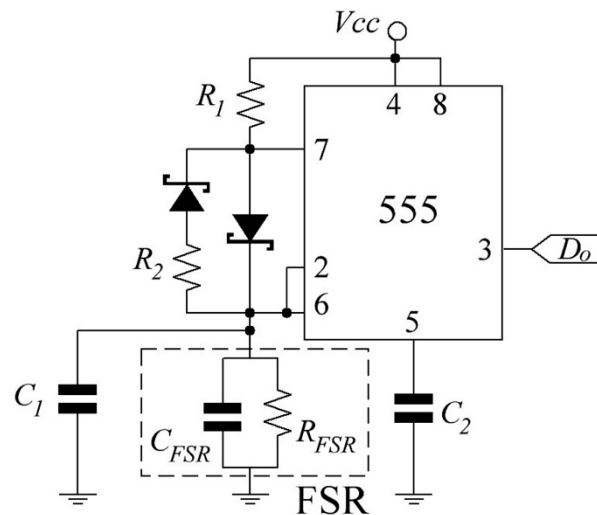

Figure 3. The authors proposed a circuit for self-compensated measurements in FSRs. The equivalent model for the FSR is enclosed within the dashed lines.

The modified-astable 555 circuit in Figure 3 imposes a time constant (τ) of $\tau_{on} = C_e \cdot R_{FSR} \cdot R_1 / (R_1 + R_{FSR})$ for the charge phase, and $\tau_{off} = C_e \cdot R_{FSR} \cdot R_2 / (R_2 + R_{FSR})$ for the discharge phase, where C_e is given by $C_e = C_1 + C_{FSR}$. The resistances R_1 and R_2 have the role of reducing the larger creep in R_{FSR}. Readers can verify that if R_{FSR} drifts to a certain amount, then $R_{FSR} \cdot R_1 / (R_1 + R_{FSR})$ and $R_{FSR} \cdot R_2 / (R_2 + R_{FSR})$ always creep less in the same time lapse. The resistances R_1 and R_2 are henceforth designated as the parallel-offset resistances. For instance, if R_{FSR} is heavily offset, it implies that the parallel connection between R_1 and R_{FSR} is dominated by R_1. Conversely, if R_1 and R_{FSR} are comparable, then R_{FSR} is slightly offset.

The optional capacitance C_1 has the role of lowering the oscillation frequency. As later demonstrated in Section 4, *f* results in the order of several hundred kilohertz which can be too high for some measuring circuits.

In order to understand how drift compensation is achieved, it is necessary to find expressions for the charge and discharge times of C_e. The time required for C_e to charge from $1/3 \cdot Vcc$ to $2/3 \cdot Vcc$ can be found from the expression

$$t_{on} = C_e \frac{R_{FSR} R_1}{R_{FSR} + R_1} \ln \left(\frac{1/3 - R_{FSR}/(R_1 + R_{FSR})}{2/3 - R_{FSR}/(R_1 + R_{FSR})} \right), \tag{11}$$

and the time required for C_e to discharge from $2/3 \cdot Vcc$ to $1/3 \cdot Vcc$ is

$$t_{off} = C_e \frac{R_{FSR} R_2}{R_{FSR} + R_2} \ln(2) \tag{12}$$

However, Equation (11) can be further simplified with an admissible error by noticing that R_{FSR} is, in practice, many times larger than R_1, and thus, $R_{FSR}/(R_1 + R_{FSR}) \approx 1$. This is later demonstrated in Section 4. By replacing $R_{FSR}/(R_1 + R_{FSR}) = 1$ in Equation (11), t_{on} can be approximated to

$$t_{on} \approx C_e \frac{R_{FSR}R_1}{R_{FSR} + R_1} \ln(2) \tag{13}$$

3.1. Compensation Mechanism Using $R_1 = R_2$

In a first attempt—and for simplification purposes—the resistances R_1 and R_2 are set to be equal so that a single time constant is obtained for the charge and the discharge phases. Based on this assumption, $R_1 = R_2$, the time constant is given by $\tau = R_e \cdot C_e$, where $R_e = R_{FSR} \cdot R_1/(R_1 + R_{FSR})$. From this observation, t_{on} and t_{off} are identical and the design criteria for drift compensation relies solely on the time constant as follows:

$$\tau = R_e C_e = (R_e - \varepsilon_R)(C_e + \varepsilon_C), \tag{14}$$

where ε_R and ε_C are the small variations in the sensor's resistance and capacitance, respectively, due to creep in the inter-particle separation, $s(\sigma,t)$.

An explanation for the opposite signs of ε_R and ε_C was already presented in Section 2.3 but it can be summarized as follows. The symbol "$-\varepsilon_R$" is negative because the creep in $s(\sigma,t)$ yields a lower resistance just as Equation (2) and Equations (4)–(6) predict. The symbol "ε_C" is positive because the creep in $s(\sigma,t)$ yields a larger capacitance as predicted by Equation (9). Finally, Equation (14) may be understood as follows: in order to compensate for the creep in $s(\sigma,t)$, the time constant of the circuit must remain unchanged; this can be achieved from the opposite creep characteristic of the sensor's resistance and capacitance. If $R_1 = R_2$, the resulting frequency, f, in D_0 can be approximately found from Equations (12) and (13) as next:

$$f = \left(t_{on} + t_{off}\right)^{-1} \approx (2C_e R_e \ln(2))^{-1} \tag{15}$$

3.2. Compensation Mechanism Using $R_1 \neq R_2$

A more accurate and general expression for f can be found on the basis of first, setting different values for R_1 and R_2, and second, using Equations (11) and (12) for t_{on} and t_{off} as follows:

$$f = \cfrac{1}{C_e \left\{ \cfrac{R_{FSR}R_2 \ln(2)}{R_{FSR} + R_2} + \cfrac{R_{FSR}R_1}{R_{FSR} + R_1} \ln\left(\cfrac{\frac{1}{3} - \frac{R_{FSR}}{(R_1 + R_{FSR})}}{\frac{2}{3} - \frac{R_{FSR}}{(R_1 + R_{FSR})}} \right) \right\}} \tag{16}$$

Nonetheless, Equation (16) is still an approximated expression because it does not take into consideration the voltage-dependent behavior of R_{FSR}; see Figure 2 and Equations (4)–(6). For this reason, if Vcc is changed in the circuit in Figure 3, the resulting frequency is changed as well. This may seem to be a drawback of the authors' proposed circuit, but it must be recalled that the manufacturer's recommended circuit exhibits the same behavior in regard to V_o measurements [11].

If R_1 and R_2 are set different, the compensation mechanism is the same as that of Equation (14), but in this case, a degree of freedom is gained since R_1 and R_2 can be independently trimmed. The analytical calculation for the optimal values of R_1 and R_2 is challenging for two reasons: first, R_{FSR} is voltage-dependent, and second, R_{FSR} notably changes from one specimen to another. For these reasons, the optimal values of R_1 and R_2 were found in this study by following an empirical approach. It is later demonstrated that the design criteria from Equation (14) also minimizes the hysteresis in frequency readings.

4. Experimental Setup, Results, and Discussion

At this point, it must be highlighted that this study initially considered the usage of both FlexiForce and Interlink sensors. However, the Interlink sensors are manufactured using Non-Aligned Electrodes Element (NAEE) [15]; the NAEE configuration uses interdigitated electrodes in opposition to the Traditional Sandwich Element (TSE) in Figure 1a. The TSE configuration is employed by the FlexiForce sensors. The NAEE configuration avoids the formation of lumped capacitances, and thus, the Interlink sensors exhibited negligible and stress-independent C_{FSR}. For this reason, the Interlink sensors could not be tested with the circuit in Figure 3.

The experimental setup comprised a tailored test bench for applying static and dynamic loads and two electrical circuits for collecting the sensors' resistance and resulting frequency. A detailed description of the mechanical test bench has been presented by the authors in Reference [37], so only a brief description is next presented. The mechanical test bench is capable of handling multiple sensors using a sandwich-like configuration, see Figure 4. Forces are applied through a linear motor with a load cell as a reference to close the force loops. The sensors' holders have a notch on the upper side for avoiding the undesired displacement of the sensors, and a puck on the lower side for applying stress in an evenly distributed manner. The pucks are round with a diameter of 7.7 mm.
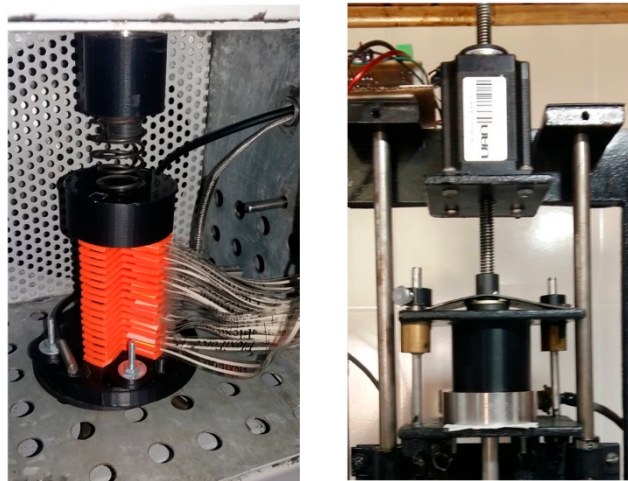

Figure 4. The mechanical setup for collecting the sensors' data. (**Left**) Multiple FSRs are arranged using a sandwich-like configuration. Mechanical compliance is provided by a spring; (**Right**) Forces are applied through a linear motor and force loops are closed using a load cell.

The electrical setup comprised of two circuits: an amplifier in inverting configuration to readout sensor's resistance, and the authors' proposed circuit in Figure 3. The amplifier sketch is shown in Figure 5, this is the manufacturer's recommended circuit which is henceforth used as a reference for error comparison [11]. Given the amplifier in Figure 5 with sourcing V_{FSR}, the sensor's resistance, R_{FSR}, can be estimated from the following formula:

$$R_{FSR} = -V_{FSR}R_f/V_o, \tag{17}$$

where R_f and V_o are the feedback resistor and the output voltage, respectively. The circuits shown in Figures 3 and 5 can drive a single FSR, but multiple FSRs can be simultaneously handled if multiplexers are employed [22,37].

Before proceeding with the experimental results, it is necessary to discuss the relationship between the applied stress, σ, and the parameters s, R_{FSR}, C_{FSR}, and f. The inter–particle separation, s, is reduced for larger stresses, and consequently, Equation (2) and Equations (4)–(6) predict a lower R_{FSR} for incremental stresses. Conversely, C_{FSR} grows for larger σ as predicted by Equation (9).

The experimental data of R_{FSR} as a function of σ is shown in Figure 6a for the FlexiForce A201-25 sensor at multiple V_{FSR}. Note that R_{FSR} is influenced by V_{FSR} as predicted by the simulation plot in Figure 2 and Equations (4)–(6).
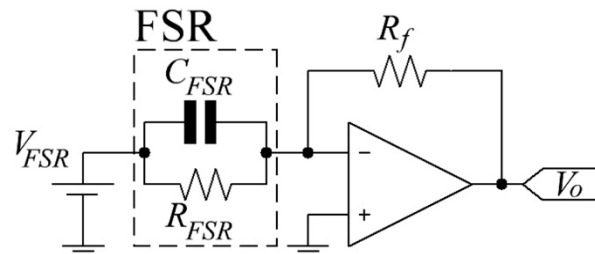

Figure 5. The manufacturer's recommended method for measuring the sensor's resistance (R_{FSR}) based on an amplifier in an inverting configuration [11].

Figure 6b shows the experimental data for the resulting frequency, f, as a function of σ at multiple Vcc for $R_1 = R_2 = 2.2$ kΩ. From this plot, several facts can be deduced. First, the larger Vcc is, the higher f becomes; this is because R_{FSR} is lowered with larger V_{FSR}, thus reducing the time constant. Second, larger stresses yield lower frequencies; this is because the predominant sensing mechanism for a heavily offset sensor is capacitance and not resistance. In other words, considering that $R_1 = R_2 = 2.2$ kΩ, the parallel connection between R_1 and R_{FSR} is dominated by R_1, and therefore, the resulting frequency is predominantly modified by C_e; see Equation (15). Note from Figure 6a that R_{FSR} is usually within the range of several tens of kilo-Ohms. And third, the resulting frequency does not linearly change with stress because C_{FSR} changes with the square root of σ. This study does not present the experimental data of the sensor's capacitance, but previous authors' work does [30].
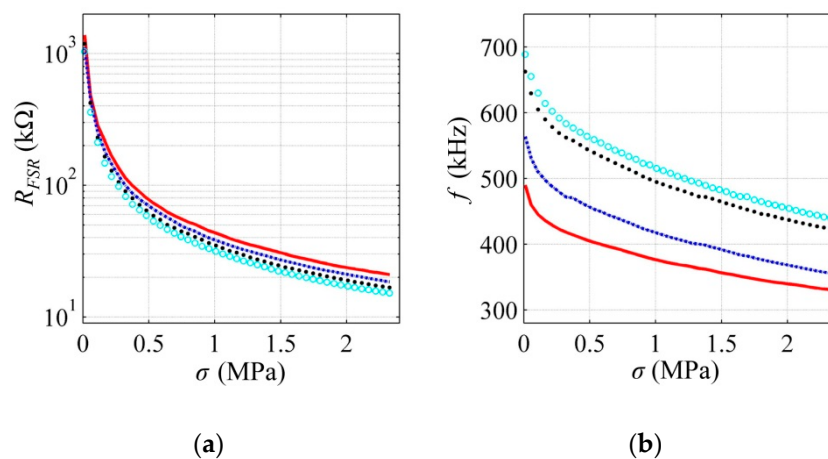

(a)   (b)

Figure 6. The plots of the sensor's resistance (R_{FSR}) and resulting frequency (f) as a function of the applied stress (σ) for the FlexiForce A201-25 sensor. (**a**) R_{FSR} measured from the circuit in Figure 5 and Equation (17) at multiple voltages, $V_{FSR} = 1.25$ V (solid red), $V_{FSR} = 2.5$ V (dashed blue), $V_{FSR} = 3.75$ V (black points), $V_{FSR} = 5$ V (circle cyan); (**b**) f measured from the circuit in Figure 3 with $R_1 = R_2 = 2.2$ kΩ at multiple sourcing voltages, $Vcc = 2.5$ V (solid red), $Vcc = 3.5$ V (dashed blue), $Vcc = 4.5$ V (black points), $Vcc = 5.5$ V (circle cyan).

4.1. Trimming the Offset Resistances for $R_1 = R_2$

The box plots from this Section report on the experimental data from the eight FlexiForce A201-25 sensors under study. Figure 7 shows box plots for the drift in the resulting frequency at different offset resistances with $R_1 = R_2$. The data were taken at stresses of 2.3 MPa, 1.15 MPa, and 0.23 MPa that

account for 100%, 50%, and 10% of the nominal sensor range, respectively. *Vcc* was set to 2.5 V in this test; see the driving circuit in Figure 3.
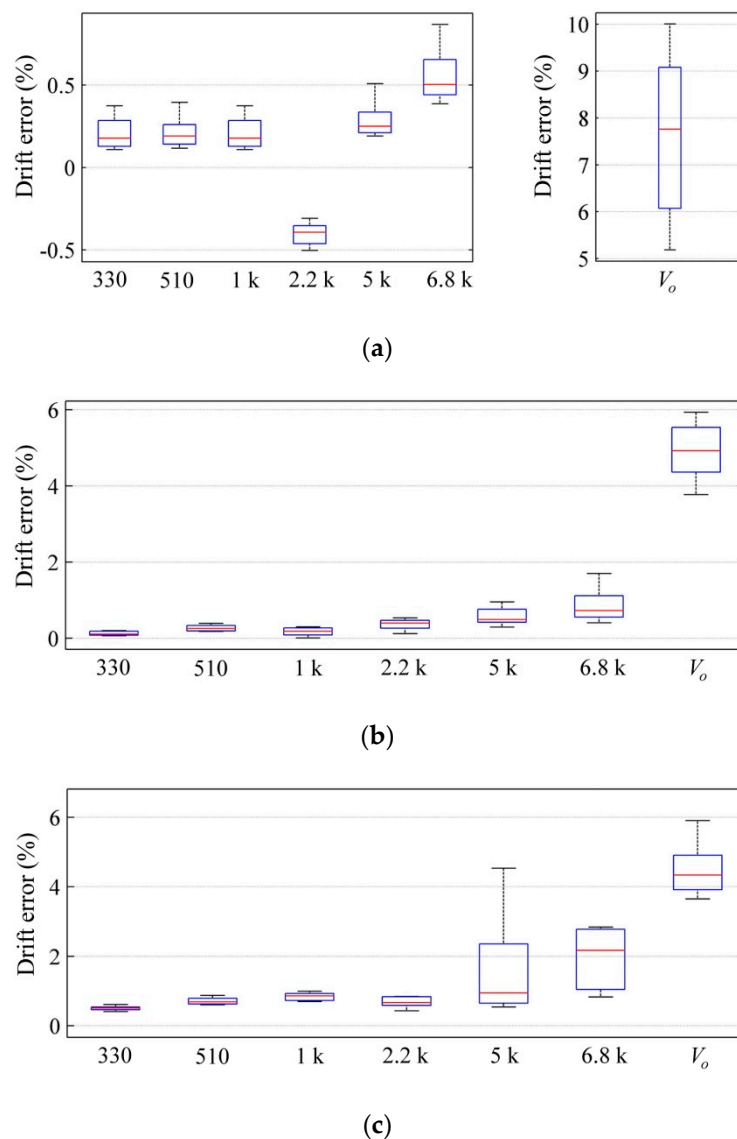

(**a**)

(**b**)

(**c**)

Figure 7. The box plots of the drift in the amplifier output voltage (V_o) and the resulting frequency (f) at different stresses (σ). The drift estimated after one hour of operation on the basis of Equations (18) and (19) for V_o and f measurements, respectively. The sourcing voltages were set to $V_{FSR} = 1.25$ V and $Vcc = 2.5$ V according to the circuits in Figures 3 and 5, respectively. The x-axis of the plots represent the offset resistances employed during each test with $R_1 = R_2$ and the traditional method (V_o) at (**a**) $\sigma = 2.3$ MPa, (**b**) $\sigma = 1.15$ MPa, and (**c**) $\sigma = 0.23$ MPa.

The sensors were also tested on the basis of the manufacturer's recommended circuit (see Figure 5) at the aforementioned stresses with $V_{FSR} = 1.25$ V. However, in this case, the drift errors were calculated from V_o and not from R_{FSR}; this was done so because V_o and σ are linearly correlated, thus V_o is the preferred parameter in the literature to determine the stress [8,38]. The drift errors in Figure 7 were estimated at $t = 3600$ s using the following formulas:

$$drift\_V_o(t) = \frac{V_o(t) - V_o(0)}{V_o(0)} \times 100\% \qquad (18)$$

$$drift\_f(t) = \frac{f(0) - f(t)}{f(0)} \times 100\% \tag{19}$$

A sign change was required in Equation (19) due to the inverse proportionality between f and σ; see Figure 6b, i.e., a positive drift in Equations (18) and (19) imply that the measured stress grows over time.

Hysteresis errors were also calculated for V_o and f at multiple offset resistances. Box plots for the hysteresis errors are shown in Figure 8.
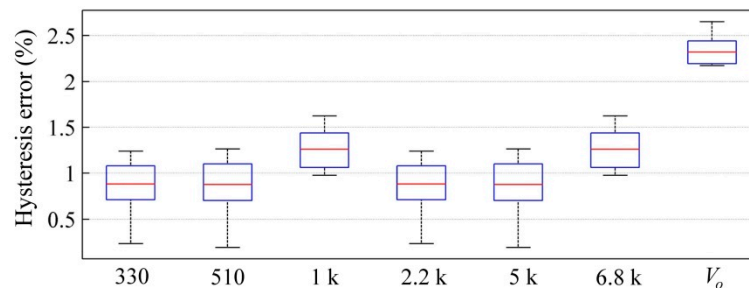

Figure 8. The box plot of the hysteresis error obtained from the authors' proposed circuit in Figure 3, and the manufacturer's recommended method in Figure 5. The x-axis of the plot represents the offset resistances employed during each test with $R_1 = R_2$ and the traditional method (V_o).

According to Figure 7, a dramatic reduction in the drift error was observed between the authors' proposed circuit in Figure 3, and the manufacturer's recommended method in Figure 5. Considerable reduction in the hysteresis error is also reported in Figure 8. Nonetheless, this is not surprising since previous authors' work has demonstrated that C_{FSR} measurements yield lower drift and hysteresis errors [21,22]. This statement is also supported by the inequality of Equation (10).

Error reduction is greater for the offset resistances within the range 330 Ω–2.2 kΩ, but still, a full compensation of drift or hysteresis was not obtained. Likewise, note that the sign change is never observed in the drift characteristic with the exception in Figure 7a at $R_1 = R_2 = 2.2$ kΩ. The drift error is mostly always positive thus indicating that "ε_C" dominates in Equation (14), i.e., even for large values of R_1, the drift compensation is never dominated by "$-\varepsilon_R$", but instead, the drift error turns even greater as R_1 is gradually incremented. This may seem as a contradiction at a glance, but it can be explained by recalling that the derivation from Section 3.1 was obtained on the basis of assuming that R_{FSR} is many times larger than R_1, see Equation (13). If R_1 is comparable with R_{FSR}, the approximated formula from Equation (15) cannot be taken as valid, and Equations (11) and (12) and Equation (16) should be used instead.

Unfortunately, if $R_1 = R_2$ with R_1 comparable to R_{FSR}, the compensation criteria from Equation (14) cannot be fully satisfied because t_{on} in Equation (11) is modified by R_1 in a two-folded way, by the parallel connection between R_1 and R_{FSR}, and by the argument of the natural logarithm. For incremental values of R_1, one term grows and the other decreases, thus limiting the offset effect of R_1 in the compensation network. In order to obtain a full compensation of the drift, it is mandatory to independently set R_1 and R_2.

4.2. Trimming the Offset Resistances for $R_1 \neq R_2$

The offset resistances can be independently trimmed to obtain full drift compensation. The trimming procedure implies setting a fixed R_1 and experimentally trimming R_2 to satisfy the condition of Equation (14). The opposite procedure (setting R_2 and trimming R_1) is also possible, but convergence is not ensured given the double dependence on R_1 at the t_{on} expression; see Equation (11).

From the box plots in Figure 7, R_1 under 2.2 kΩ could be chosen to later trim R_2. However, it is desirable to depart from an R_1 that yields low hysteresis and drift errors. It is the user's decision to choose the most appropriate R_1 based upon the target range of *f*. The larger R_1 is, the lower the resulting frequency becomes, see Equations (11)–(16). There are multiple combinations of R_1 and R_2 that satisfy Equation (14). The authors have chosen R_1 = 510 Ω as the value to later trim R_2.

Figure 9 shows the time plots of the drift in *f* at different R_2 with errors estimated from Equation (19). The applied stress during this test was 1.15 MPa. Note that as R_2 grows, the drift characteristic is gradually dominated by "$-\varepsilon_R$", whereas the "ε_C" component is progressively diminished. In the limit case when R_2 = 1.5 kΩ, the resulting drift is negative thus indicating that "$-\varepsilon_R$" dominates.

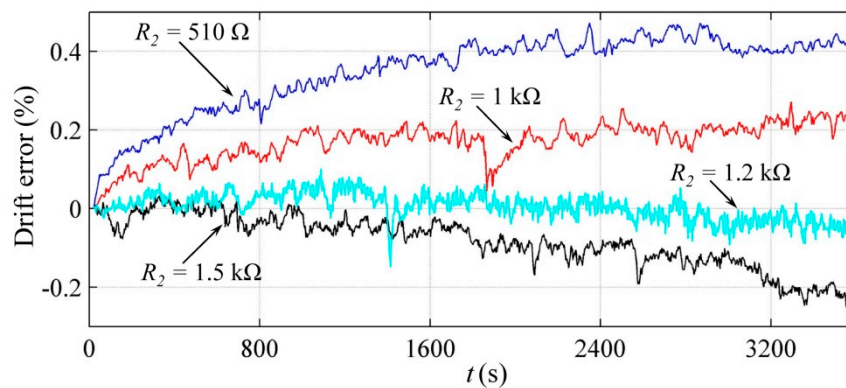**Figure 9.** The time plots of the drift in the resulting frequency measured from the circuit in Figure 3 at *Vcc* = 2.5 V, σ = 1.15 MPa using Equation (19) for error assessment. The offset resistance R_1 was fixed at 510 Ω for all tests. The offset resistance R_2 was changed between trials according to the arrow marks.

Full compensation of the error was obtained for this specimen when R_2 equals 1.2 kΩ. However, the frequency signal is somewhat noisy at 0%. The authors can only hypothesize about the possible source of the noise. The experimental observations from the previous authors' work demonstrated that the effective area for tunneling conduction, *A*, is modified by the applied stress [19]; see Equation (7). If σ is held constant for an extended period of time, the authors believe that *A* fluctuates in a random fashion, thus, causing the noise in Figure 9. It must be highlighted that *A* modifies both R_{FSR} and C_{FSR}, as predicted by Equations (4)–(6) and Equation (9). An experimental fact supports the hypothesis of a randomly fluctuating *A* as the source of the noise. If the drift experiment is repeated at the same electromechanical conditions, a somewhat different noise pattern is observed. To the authors' criteria, this occurs because the tunneling paths can be created or destroyed over time amidst a constant σ. Each specimen of FlexiForce A201-25 sensor exhibited a different R_2 for obtaining full drift compensation.

It is logical to suppose that the noise in Figure 9 is produced by the random behavior of the inter-particle separation. Nonetheless, to the authors' criteria, this is quite unlikely to happen, because σ and *s* are correlated by rheological models which are non-negative functions [31], and therefore, the negative phase of *drift_f* cannot originate from an increment of *s* amidst constantly applied stress.

The authors do pay a lot of attention to the electrical noise in Figure 9 because it may indicate that the theoretical limit of accuracy has been reached for the FlexiForce A201-25 sensor, i.e., Figure 9 indicates that no matter what the compensation network is, the measuring uncertainty is held around 0.1% of the applied stress. Reducing the noise in FSRs is also an active research trend. For instance, Wang and Li have demonstrated that the vulcanization of the sensor's electrodes is an effective method for reducing noise in such devices [39]. Nonetheless, it must be remarked that a measuring uncertainty of 0.1% is a very good result considering that a repeatability error of 2.5% has been stated in the sensor's datasheet [11].

A comprehensive model has been developed by Sheng [40] for the electrical noise in tunneling conduction. Given the small number of free electrons in the conductive nanoparticles, they result in being very sensitive to the transient deficits or excesses of charges. When this occurs, voltage fluctuations appear across the multiple tunneling paths, causing electrical noise.

4.3. Testing the Authors' Proposed Circuit

In order to comparatively test the authors' proposed circuit with the manufacturer's recommended method, the following test signal was applied to the sensors for a time span of five hours:

$$\sigma(t) = \left(1.26 + 1.05\sin(2 \times 10^{-2}t)\right) \text{MPa} \tag{20}$$

The dynamic signal from Equation (20) aims to test the sensors in a comprehensive way. The occurrence of sensitivity degradation is assessed through the sine component. Likewise, drift is also evaluated since the smallest value of stress is 0.21 MPa in Equation (20), which corresponds to a minimum force of 9.8 N.

Figure 10a–c show the time plots of the resulting frequency for different values of R_1, R_2, and Vcc. The manufacturer's recommended method was also tested with the stress signal of Equation (20) at $V_{FSR} = 1.25$ V; see Figure 10d. The plots in Figure 10 show the experimental data for a single specimen of the FlexiForce A201-25 sensor, but the statistical data from the eight specimens are presented in Table 1 using the Root Mean Squared Error (RMSE) as the metric to assess the performance of each method. In order to obtain the RMSE, the f–σ curve of each sensor was fitted to a third-order polynomial function and then, the applied stress was estimated from the frequency measurements. On the other hand, the stress estimation in Figure 10d was possible from a first-order polynomial fit on the basis of V_o measurements.

Given the f and V_o measurements, and the polynomial models, the measured stress (σ_{meas}) could be computed for each method. The RMSE was later calculated by taking the load cell data from Figure 4 as the reference for the error calculation.

The smallest RMSE was obtained for the experimental set up with $R_1 = 510\ \Omega$, $R_2 = 1.2\ \text{k}\Omega$, and $Vcc = 2.5$ V (Figure 10b); this is not surprising given the fine-tuning presented in Figure 9. The experimental setup with $R_1 = R_2 = 510\ \Omega$ (Figure 10a) exhibited a somewhat larger RMSE, but still, the resulting RMSE is almost four times lower than the error resulting from the manufacturer's recommended method in Figure 10d. It must be recalled that the resistance drift is always larger than the capacitance drift—see Equation (10)—and consequently, the circuit in Figure 3 always yields a lower RMSE because frequency variations are predominantly modified by capacitance changes.

The plot in Figure 10c exhibited sensitivity degradation, and therefore, the largest RMSE was obtained with this experimental setup. Sensitivity degradation was not observed in Figure 10d because V_{FSR} was held low at 1.25 V. Readers may refer to References [32,35,36] for experimental results showing the sensitivity degradation for the setup in Figure 5.

The experimental results in Figure 10 and Table 1 demonstrate that the authors' proposed circuit is an effective method for reducing the measurement errors in FSRs.

Table 1. The Root Mean Squared Error (RMSE) for multiple experimental setups to test the signal given by Equation (20).

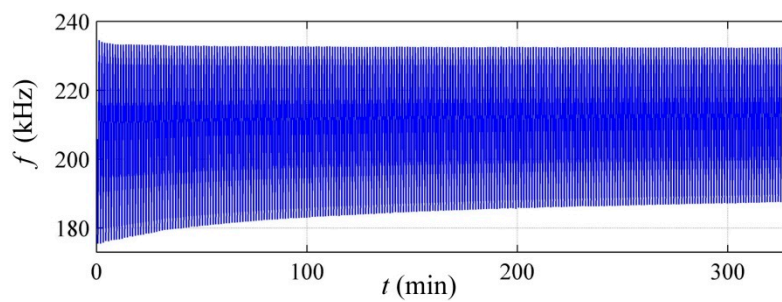| Experimental Setup in Figure 10	(a) [1]	(b) [1]	(c) [1]	(d) [2]
RMSE (kPa)	115	75.2	749	451

[1] Experimental setups based on the authors' proposed circuit of Figure 3. (a) $R_1 = R_2 = 510\ \Omega$, $Vcc = 2.5$ V. (b) $R_1 = 510\ \Omega$, $R_2 = 1.2\ \text{k}\Omega$ with $Vcc = 2.5$ V. (c) $R_1 = R_2 = 5\ \text{k}\Omega$ with $Vcc = 10$ V. [2] Experimental setup based on the manufacturer's recommended method in Figure 5 with $V_{FSR} = 1.25$ V.
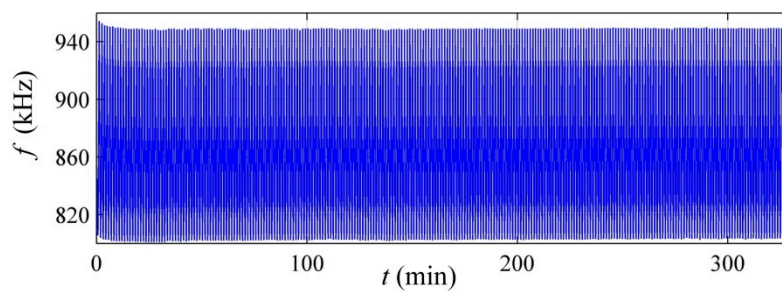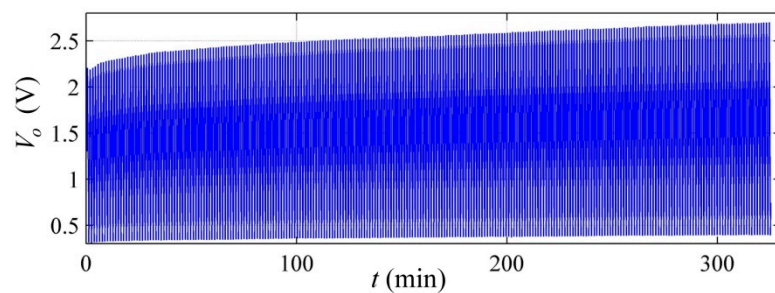
(**a**)
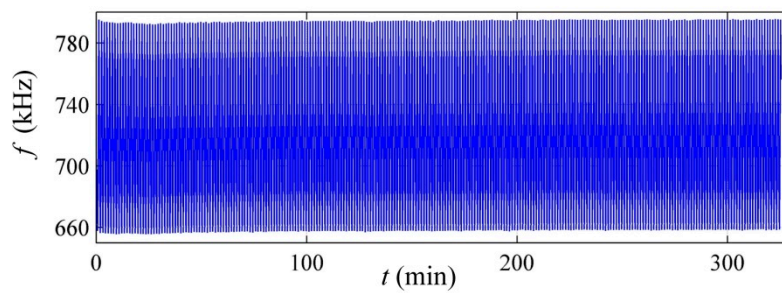
(**b**)

(**c**)

(**d**)

Figure 10. The experimental results of sensor testing using the stress signal of Equation (20) and different experimental setups. The authors' proposed circuit in Figure 3 at (**a**) $R_1 = R_2 = 510\ \Omega$ with $Vcc = 2.5$ V; (**b**) $R_1 = 510\ \Omega$, $R_2 = 1.2$ kΩ with $Vcc = 2.5$ V; (**c**) $R_1 = R_2 = 5$ kΩ with $Vcc = 10$ V; (**d**) The manufacturer's recommended method from Figure 5 with $V_{FSR} = 1.25$ V.

4.4. Comparing the Performance of the Authors' Proposed Circuit with Manufacturer Data (datasheet)

Providing a comparison with manufacturer data may result confusing because the manufacturer does not specify the full test conditions in the sensor's datasheet [11]. In previous studies, the authors have demonstrated the influence of the sourcing voltage on the sensor's performance [19,20]. Unfortunately, the sensor's datasheet only specifies the mechanical conditions when the sensor's performance was evaluated [11]. Table 2 provides a comparison among three different sources: the authors' proposed circuit in Figure 3, the sensor's datasheet [11], and previous experimental data from the circuit in Figure 5 at multiple voltages [20]; it must be remarked that the circuit in Figure 5 is the same employed in the sensor's datasheet.

Table 2. The comparative performance of the authors' proposed circuit with information from the sensor's datasheet [11]. Previous authors' data are also reported for comparison purposes [20].

Experimental Setup	Authors' Proposed Circuit in Figure 3	Sensor's Datasheet [11]	Previous Authors' Data [20] Using the Circuit in Figure 5
Hysteresis Error	[1] lower than 1.25%	[3] lower than 4.5%	not studied
Drift Error	[2] 0.5% for σ = 2.3 MPa 0.6% for σ = 1.15 MPa 2.1% for σ = 0.23 MPa	[4] lower than 5% per logarithmic time scale	[5] 3.8% for V_{FSR} = 0.5 V 3.1% for V_{FSR} = 1 V 1.9% for V_{FSR} = 3 V 0.5% for V_{FSR} = 6 V −0.5% for V_{FSR} = 9 V

[1] Data were taken from Figure 8 for the FlexiForce A201-25 with Vcc = 2.5 V; [2] Data were taken from Figure 7 for the FlexiForce A201-25 with Vcc = 2.5 V; [3] Measured at 80% of the full force applied, unknown voltage; [4] Constant load of 111 N for the FlexiForce A201-25, unknown voltage; [5] Constant load of 210 kPa applied to the FlexiForce A201-1, drift measured after one hour.

5. Conclusions

Force Sensing Resistors (FSRs) exhibit an opposite sign in the drift characteristic of sensors' resistance and capacitance. This behavior can be used to design a self-compensated driving circuit. The proposed compensation method is based on a modified-astable 555 circuit in which the FSR was configured to charge and discharge in an oscillating basis. Given the larger drift in the sensor's resistance, it has been conveniently offset to match the lower drift in the sensor's capacitance; this was done from a fixed resistance connected through the charge and discharge paths.

Experimental results of the modified-astable 555 circuit yielded a dramatic reduction of the drift and hysteresis errors (by a factor of 9 in the drift error and a factor of 3 in the hysteresis error) when compared with the manufacturer's recommended method, which is based on an amplifier in the inverting configuration.

The output frequency (*f*) of the modified-astable 555 circuit was successfully correlated with the applied stress (σ). This allowed for the estimation of unknown stresses on the basis of *f* measurements. The *f*-σ relationship was not linear, and therefore, a third-order polynomial fit was required for this purpose.

Author Contributions: J.F. and A.M. designed and built the PCB for circuit testing. E.I.G.V. designed and built the mechanical setup. L.P.-M. and C.A.P. wrote the paper.

Conflicts of Interest: The authors declare no conflict of interest.

Appendix

Figure A1 presents a comparison between the modified-astable 555 circuit and the classical version of the astable circuit. The modified-astable 555 circuit provides a self-compensation mechanism for the drift and hysteresis error in FSRs. The charge and discharge equivalent circuits are also presented in Figure A1 for comparison purposes.
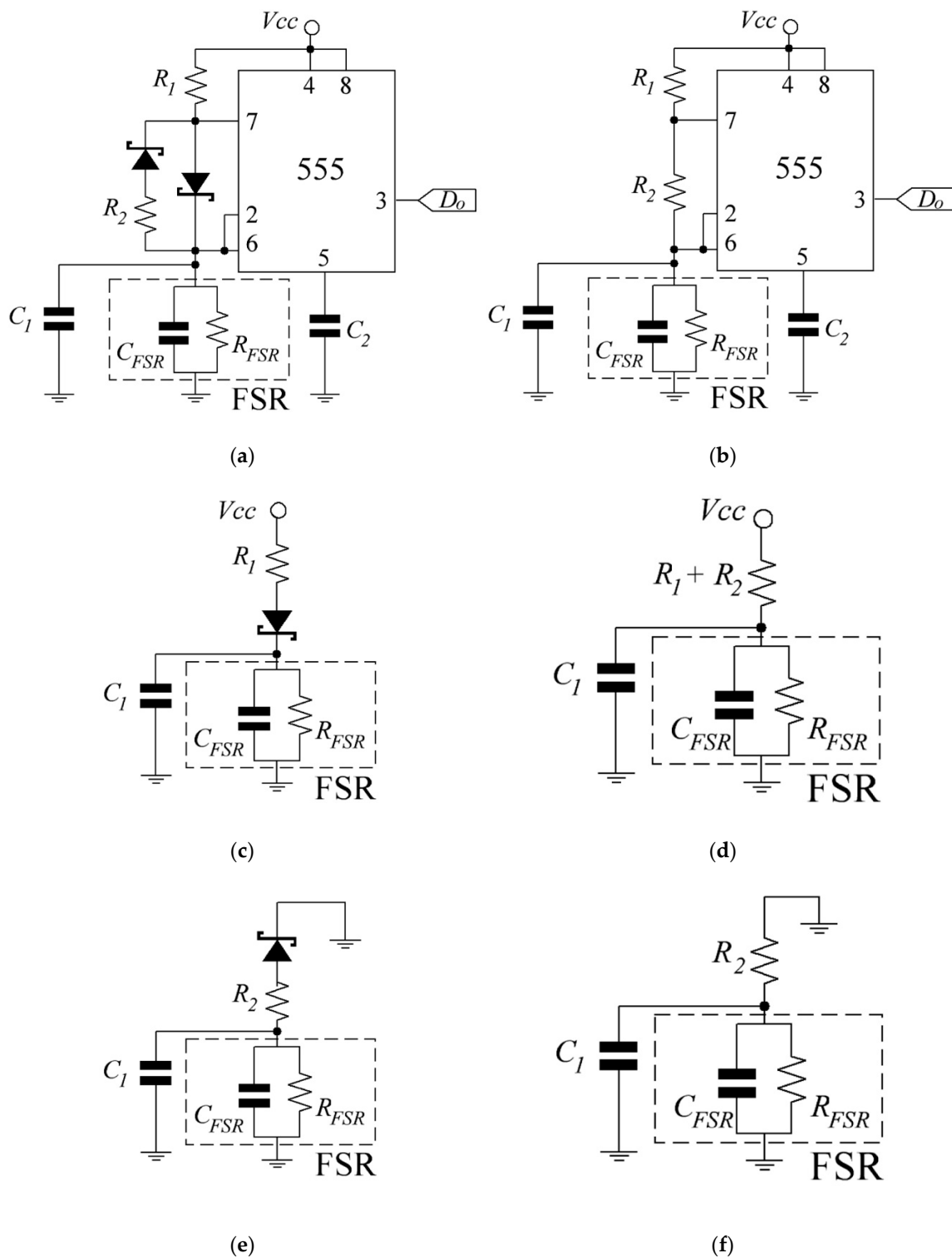
Figure A1. The classical-astable and modified-astable 555 circuits. (**a**) modified-astable 555 circuit for compensating drift and hysteresis in FSRs; (**b**) Classical-astable circuit shown in the datasheet [41]; (**c**) Equivalent charge circuit of the modified-astable 555; (**d**) Equivalent charge circuit of the classical-astable 555; (**e**) Equivalent discharge circuit of the modified-astable 555; (**f**) Equivalent discharge circuit of the classical-astable 555.

Equations for the charge and discharge phases of the modified-astable 555 circuit have been previously presented in Section 3. Therefore, in this appendix, only the equations for the classical 555

are introduced. However, the expressions presented next are intrinsically different from the well-known formulas in the literature; this is because of the sensor's resistance, R_{FSR}, which is connected in parallel with C_{FSR}. The charge time (t_{on}) for the circuit in Figure A1d can be found from

$$t_{on} = C_e \frac{R_{FSR}(R_1 + R_2)}{R_{FSR} + R_1 + R_2} \ln\left(\frac{1/3 - R_{FSR}/(R_1 + R_2 + R_{FSR})}{2/3 - R_{FSR}/(R_1 + R_2 + R_{FSR})}\right) \tag{A1}$$

Equation (A1) is comparable to Equation (11). An expression for the discharge phase (t_{off}) of the circuit in Figure A1f can be found from

$$t_{off} = \ln(2)(C_1 + C_{FSR}) \frac{R_2 R_{FSR}}{R_2 + R_{FSR}} \tag{A2}$$

Finally, Equation (A2) is comparable to Equation (12). In this case, Equations (A2) and (12) are the same if the voltage drop across the Schottky diode is neglected; compare Figure A1e with Figure A1f.

References

1. Bianchi, M.; Haschke, R.; Büscher, G.; Ciotti, S.; Carbonaro, N.; Tognetti, A. A multi-modal sensing glove for human manual-interaction studies. *Electronics* **2016**, *5*, 42. [CrossRef]
2. Ramirez-Bautista, J.A.; Huerta-Ruelas, J.A.; Chaparro-Cárdenas, S.L.; Hernández-Zavala, A. A review in detection and monitoring gait disorders using in-shoe plantar measurement systems. *IEEE Rev. Biomed. Eng.* **2017**, *10*, 299–309. [CrossRef] [PubMed]
3. Carbonaro, N.; Lorussi, F.; Tognetti, A. Assessment of a smart sensing shoe for gait phase detection in level walking. *Electronics* **2016**, *5*, 78. [CrossRef]
4. Castellanos-Ramos, J.; Navas-Gonzalez, R.; Macicior, H.; Sikora, T.; Ochoteco, E.; Vidal-Verdu, F. Tactile sensors based on conductive polymers. *Microsyst. Technol.* **2010**, *16*, 765–776. [CrossRef]
5. Bloor, D.; Donnelly, K.; Hands, P.J.; Laughlin, P.; Lussey, D. A metal-polymer composite with unusual properties. *J. Phys. D Appl. Phys.* **2005**, *38*, 2851. [CrossRef]
6. Wang, L.; Ding, T.; Wang, P. Influence of carbon black concentration on piezoresistivity for carbon-black-filled silicone rubber composite. *Carbon* **2009**, *47*, 3151–3157. [CrossRef]
7. Vidhate, S.; Chung, J.; Vaidyanathan, V.; D'Souza, N.A. Resistive-conductive transitions in the time-dependent piezoresponse of PVDF-MWCNT nanocomposites. *Polym. J.* **2010**, *42*, 567–574. [CrossRef]
8. Hidalgo-Lopez, J.A.; Oballe-Peinado, O.; Castellanos-Ramos, J.; Sanchez-Duran, J.A.; Fernandez-Ramos, R.; Vidal-Verdu, F. High-accuracy readout electronics for piezoresistive tactile sensors. *Sensors* **2017**, *17*, 2513. [CrossRef] [PubMed]
9. Zhou, J.F.; Song, Y.H.; Zheng, Q.; Wu, Q.; Zhang, M.Q. Percolation transition and hydrostatic piezoresistance for carbon black filled poly(methylvinylsilioxane) vulcanizates. *Carbon* **2008**, *46*, 679–691. [CrossRef]
10. Hussain, M.; Choa, Y.H.; Niihara, K. Conductive rubber materials for pressure sensors. *J. Mater. Sci. Lett.* **2001**, *20*, 525–527. [CrossRef]
11. Tekscan Inc. FlexiForce, Standard Force & Load Sensors Model A201. Available online: https://www.tekscan.com/sites/default/files/resources/FLX-A201-A.pdf (accessed on 16 June 2017).
12. Interlink Electronics. FSR400 Series Datasheet. Camarillo, CA 93012, USA. Available online: http://www.interlinkelectronics.com/datasheets/Datasheet_FSR.pdf (accessed on 16 June 2017).
13. Peratech Holdco Limited. QTC SP200 Series Datasheet Single Point Sensors. Available online: https://www.peratech.com/assets/uploads/datasheets/Peratech-QTC-DataSheet-SP200-Series-Nov15.pdf (accessed on 17 July 2017).
14. Sanli, A.; Benchirouf, A.; Müller, C.; Kanoun, O. Piezoresistive performance characterization of strain sensitive multi-walled carbon nanotube-epoxy nanocomposites. *Sens. Actuators A* **2017**, *254*, 61–68. [CrossRef]
15. Wang, L.; Han, Y.; Wu, C.; Huang, Y. A solution to reduce the time dependence of the output resistance of a viscoelastic and piezoresistive element. *Smart Mater. Struct.* **2013**, *22*, 075021. [CrossRef]
16. Wang, L. Piezoresistive sensor based on conductive polymer composite with transverse electrodes. *IEEE Trans. Electron Devices* **2015**, *62*, 1299–1305. [CrossRef]

17. Rizvi, R.; Cochrane, B.; Biddiss, E.; Naguib, H. Piezoresistance characterization of poly(dimethyl-siloxane) and poly(ethylene) carbon nanotube composites. *Smart Mater. Struct.* **2011**, *20*, 094003. [CrossRef]

18. Stassi, S.; Cauda, V.; Canavese, G.; Pirri, C.F. Flexible tactile sensing based on piezoresistive composites: A review. *Sensors* **2014**, *14*, 5296–5332. [CrossRef] [PubMed]

19. Paredes-Madrid, L.; Palacio, C.A.; Matute, A.; Parra Vargas, C.A. Underlying physics of conductive polymer composites and force sensing resistors (FSRs) under static loading conditions. *Sensors* **2017**, *17*, 2108. [CrossRef] [PubMed]

20. Paredes-Madrid, L.; Matute, A.; Bareño, J.O.; Parra Vargas, C.A.; Gutierrez Velásquez, E.I. Underlying physics of conductive polymer composites and force sensing resistors (FSRs). A study on creep response and dynamic loading. *Materials* **2017**, *10*, 1334. [CrossRef] [PubMed]

21. Matute, A.; Paredes-Madrid, L.; Gutierrez, E.; Vargas, C.A.P. Characterization of drift and hysteresis errors in force sensing resistors considering their piezocapacitive effect. In Proceedings of the 2017 IEEE SENSORS Conference, Glasgow, UK, 29 October–1 November 2017; pp. 1–3.

22. Matute, A.; Paredes-Madrid, L.; Moreno, G.; Cardenas, F.; Palacio, C.A. A novel and inexpensive approach for force sensing based on FSRs piezocapacitance aimed to hysteresis error reduction. *J. Sens.* **2018**, *2018*. [CrossRef]

23. Krivopal, B. Pressure Sensitive Ink Means, and Method of Use. U.S. Patent 5,989,700, 23 November 1999.

24. Oreper, B.; Brenneman, J. Pressure Sensor. U.S. Patent 6,272,936, 14 August 2001.

25. Zhang, X.W.; Pan, Y.; Zheng, Q.; Yi, X.S. Time dependence of piezoresistance for the conductor-filled polymer composites. *J. Polym. Sci. Part B Polym. Phys.* **2000**, *38*, 2739–2749. [CrossRef]

26. Kalantari, M.; Dargahi, J.; Kovecses, J.; Mardasi, M.G.; Nouri, S. A new approach for modeling piezoresistive force sensors based on semiconductive polymer composites. *IEEE/ASME Trans. Mechatron.* **2012**, *17*, 572–581. [CrossRef]

27. Simmons, J. Electrical tunnel effect between dissimilar electrodes separated by a thin insulating Film. *J. Appl. Phys.* **1963**, *34*, 2581–2590. [CrossRef]

28. Mikrajuddin, A.; Shi, F.G.; Kim, H.K.; Okuyama, K. Size-dependent electrical constriction resistance for contacts of arbitrary size: From Sharvin to Holm limits. *Mater. Sci. Semicond. Process.* **1999**, *2*, 321–327. [CrossRef]

29. Shi, F.G.; Abdullah, M.; Chungpaiboonpatana, S.; Okuyama, K.; Davidson, C.; Adams, J.M. Electrical conduction of anisotropic conductive adhesives: Effect of size distribution of conducting filler particles. *Mater. Sci. Semicond. Process.* **1999**, *2*, 263–269. [CrossRef]

30. Paredes-Madrid, L.; Emmi, L.; Garcia, E.; Gonzalez de Santos, P. Detailed study of amplitude nonlinearity in piezoresistive force sensors. *Sensors* **2011**, *11*, 8836–8854. [CrossRef] [PubMed]

31. Mainardi, F.; Spada, G. Creep, relaxation and viscosity properties for basic fractional models in rheology. *Eur. Phys. J. Spec. Top.* **2011**, *193*, 133–160. [CrossRef]

32. Canavese, G.; Lombardi, M.; Stassi, S.; Pirri, C.F. Comprehensive Characterization of Large Piezoresistive Variation of Ni-PDMS Composites. *Appl. Mech. Mater.* **2012**, 1336–1344. [CrossRef]

33. Ding, S.; Han, B.; Dong, X.; Yu, X.; Ni, Y.; Zheng, Q.; Ou, J. Pressure-sensitive behaviors, mechanisms and model of field assisted quantum tunneling composites. *Polymer* **2017**, *113*, 105–118. [CrossRef]

34. Lin, L.; Liu, S.; Zhang, Q.; Li, X.; Ji, M.; Deng, H.; Fu, Q. Towards tunable sensitivity of electrical property to strain for conductive polymer composites based on thermoplastic elastomer. *ACS Appl. Mater. Interfaces* **2013**, *5*, 5815–5824. [CrossRef] [PubMed]

35. Lebosse, C.; Renaud, P.; Bayle, B.; de Mathelin, M. Modeling and Evaluation of Low-Cost Force Sensors. *IEEE Trans. Robot.* **2011**, *27*, 815–822. [CrossRef]

36. Dabling, J.; Filatov, A.; Wheeler, J. Static and cyclic performance evaluation of sensors for human interface pressure measurement. In Proceedings of the 2012 Annual International Conference of the IEEE Engineering in Medicine and Biology Society, San Diego, CA, USA, 28 August–1 September 2012; pp. 162–165.

37. Paredes-Madrid, L.; Matute, A.; Peña, A. Framework for a Calibration-Less Operation of Force Sensing Resistors at Different Temperatures. *IEEE Sens. J.* **2017**, *17*, 4133–4142. [CrossRef]

38. Ferre, M.; Galiana, I.; Aracil, R. Design of a Lightweight, Cost Effective Thimble-Like Sensor for Haptic Applications Based on Contact Force Sensors. *Sensors* **2011**, *11*, 11495–11509. [CrossRef] [PubMed]

39. Wang, L.; Li, Y. A Review for Conductive Polymer Piezoresistive Composites and a Development of a Compliant Pressure Transducer. *IEEE Trans. Instrum. Meas.* **2013**, *62*, 495–502. [CrossRef]

40. Sheng, P. Fluctuation-induced tunneling conduction in disordered materials. *Phys. Rev. B* **1980**, *21*, 2180–2195. [CrossRef]

41. Texas Instruments. LM555 Timer Datasheet. Available online: http://www.ti.com/lit/ds/symlink/lm555.pdf (accessed on 5 August 2018).